Nonaqueous Synthesis of Uniform Indium Tin Oxide Nanocrystals and Their Electrical Conductivity in Dependence of the Tin Oxide Concentration

Jianhua Ba,[†] Dina Fattakhova Rohlfing,[‡] Armin Feldhoff,[‡] Torsten Brezesinski,[†] Igor Djerdj,[†] Michael Wark,[‡] and Markus Niederberger*,[†]

Max Planck Institute of Colloids and Interfaces, Research Campus Golm, D-14424 Potsdam, Germany, Institute of Physical Chemistry and Electrochemistry, University of Hannover, Callinstrasse 3-3a, D-30167 Hannover, Germany

Received March 7, 2006. Revised Manuscript Received April 8, 2006

Indium tin oxide nanoparticles with tin oxide contents varying from 2 to 30 wt % have been synthesized via a nonaqueous sol−gel procedure involving the solvothermal treatment of indium acetylacetonate and tin *tert*-butoxide in benzyl alcohol. According to powder X-ray diffraction analysis combined with Rietveld refinement all the materials are crystalline with the cubic bixbyite structure of indium oxide without any indication of SnO_2 as an additional phase. Transmission electron microscopy studies proved that the nearly spherical particles are relatively uniform in size and shape with crystallite sizes in the range of 5−10 nm. X-ray photoelectron spectroscopy results showed that the final composition of the nanoparticles coincided well with the initial indium acetylacetonate-to-tin *tert*-butoxide ratio. Furthermore, a high amount of oxygen vacancies was detected, which contribute to the good electrical conductivity of the nanoparticles. Conductivity measurements on the as-synthesized nanopowders pressed into pellets showed a maximum conductivity of 2.56 S/cm at a dopant concentration of 15 wt % and can be further increased to 52.6 S/cm upon annealing under a nitrogen atmosphere.

Introduction

Transparent conducting oxides (TCOs) are important materials for optoelectronic devices, because they combine optical transparency in the visible region with controllable electrical conductivity. The most widely used TCO in optoelectronics is tin-doped indium oxide (indium tin oxide, ITO).[1,2] This material offers the best available performance in terms of conductivity and transmission, combined with excellent environmental stability, reproducibility, and good surface morphology.[3] The fastest growing application for ITO is the flat panel display technology; however, it is also the material of choice in a number of other applications,[1,3] including functional glass,[4−7] solar cells,[8,9] and gas sensing.[10,11]

In most cases, ITO is produced in the form of thin films applying various methods such as magnetron sputtering,[3] pulsed laser deposition,[12] chemical vapor deposition,[13] and spray pyrolysis.[14] However, these techniques are highly restricted with respect to substrate structure, substrate geometry, and cost effectiveness, and therefore liquid phase processing of ITO thin films became a widely applied alternative.[2,15] Especially sol−gel approaches combined with deposition techniques such as spin- and dip-coating were highly successful in the preparation of ITO coatings.[16,17] Nevertheless, in all these cases the main problem constitutes the amorphous nature of the as-deposited ITO layers, and heat treatment at temperatures in the range of 400−700 °C is required to achieve fully crystalline films.[18] A simple answer to this problem is the wet chemical deposition of dispersions containing crystalline nanoparticles.[19,20] The work by Al-Dahoudi and Aegerter nicely illustrates the potential advantages of such processes, namely, low cost and flexibility in the choice of the geometry as well as thermal stability of

* To whom correspondence should be addressed. E-mail: markus.niederberger@mpikg.mpg.de.
† Max Planck Institute of Colloids and Interfaces.
‡ University of Hannover.

(1) Ginley, D. S.; Bright, C. *MRS Bull.* **2000**, *25*, 15−18.
(2) Minami, T. *Semicond. Sci. Technol.* **2005**, *20*, S35−S44.
(3) Lewis, B. G.; Paine, D. C. *MRS Bull.* **2000**, *25*, 22−27.
(4) Gazotti, W. A.; Casalbore-Miceli, G.; Geri, A.; Berlin, A.; De Paoli, M. A. *Adv. Mater.* **1998**, *10*, 1522−1525.
(5) Pichot, F.; Ferrere, S.; Pitts, R. J.; Gregg, B. A. *J. Electrochem. Soc.* **1999**, *146*, 4324−4326.
(6) Granqvist, C. G.; Hultaker, A. *Thin Solid Films* **2002**, *411*, 1−5.
(7) Xu, C. Y.; Liu, L.; Legenski, S. E.; Ning, D.; Taya, M. *J. Mater. Res.* **2004**, *19*, 2072−2080.
(8) Kobayashi, H.; Ishida, T.; Nakato, Y.; Tsubomura, H. *J. Appl. Phys.* **1991**, *69*, 1736−1743.
(9) Martinez, M. A.; Herrero, J.; Gutierrez, M. T. *Thin Solid Films* **1995**, *269*, 80−84.
(10) Vaishnav, V. S.; Patel, P. D.; Patel, N. G. *Thin Solid Films* **2005**, *487*, 277−282.
(11) Forleo, A.; Francioso, L.; Epifani, M.; Capone, S.; Taurino, A. M.; Siciliano, P. *Thin Solid Films* **2005**, *490*, 68−73.
(12) Zheng, J. P.; Kwok, H. S. *Appl. Phys. Lett.* **1993**, *63*, 1−3.
(13) Maruyama, T.; Fukui, K. *J. Appl. Phys.* **1991**, *70*, 3848−3851.
(14) Frank, G.; Köstlin, H. *Appl. Phys. A* **1982**, *27*, 197−206.
(15) Aegerter, M. A.; Puetz, J.; Gasparro, G.; Al-Dahoudi, N. *Opt. Mater.* **2004**, *26*, 155−162.
(16) Kundu, S.; Biswas, P. K. *Chem. Phys. Lett.* **2005**, *414*, 107−110.
(17) Epifani, M.; Diaz, R.; Arbiol, J.; Siciliano, P.; Morante, J. R. *Chem. Mater.* **2006**, *18*, 840−846.
(18) Alam, M. J.; Cameron, D. C. *Thin Solid Films* **2002**, *420−421*, 76−82.
(19) Goebbert, C.; Nonninger, R.; Aegerter, M. A.; Schmidt, H. *Thin Solid Films* **1999**, *351*, 79−84.
(20) Ederth, J.; Johnsson, P.; Niklasson, G. A.; Hoel, A.; Hultåker, A.; Heszler, P.; Granqvist, C. G.; van Doorn, A. R.; Jongerius, M. J.; Burgard, D. *Phys. Rev. B* **2003**, *68*, 155410.

10.1021/cm060548q CCC: $33.50
Published on Web 05/17/2006

Table 1. Electrical Properties and Crystallographic Characteristics of the ITO Nanoparticles Prepared from Different In-to-Sn Starting Ratios

sample	starting In-to-Sn ratio (mol)	starting SnO_2 content (wt %)	SnO_2 content in the product[a] (wt %)	crystallite size[b] (nm)	lattice parameter[c] (Å)	volume-weighted average grain size[c] (nm)	specific conductivity (S/cm)
ITO-2	53.16	2	0.71	17.9	10.1189(3)	13.7	0.348
ITO-6	17.00	6		13.9	10.126(1)	9.9	0.518
ITO-8	12.48	8		10.9	10.129(1)	9.6	0.820
ITO-10	9.77	10	9.34	12.7	10.134(1)	8.5	1.333
ITO-12	7.96	12		9.5	10.127(1)	7.9	2.041
ITO-15	6.15	15	13.93	8.9	10.127(1)	7.6	2.564
ITO-20	4.44	20		8.3	10.107(2)	5.5	0.694
ITO-25	3.33	25		8.2	10.110(2)	5.3	0.855
ITO-30	2.59	30		7.6	10.115(3)	4.4	0.508

[a] From XPS measurements. [b] XRD using the Scherrer equation [(222) reflection]. [c] By Rietveld refinement.

the substrate (i.e., allowing the use of plastic substrates).[21] However, this approach makes great demands on the properties of the ITO nanoparticles such as high electrical conductivity and high crystallinity, homogeneous composition, and uniform particle size and shape. Particle sizes below 50 nm are a prerequisite to lower the sintering temperatures and to prevent the scattering of light, so that high visible transparency is guaranteed.

There is a vast amount of literature on the synthesis of ITO nanoparticles by means of soft chemistry approaches, mainly based on coprecipitation, often followed by hydrothermal and/or thermal treatments.[19,22,23] However, to the best of our knowledge the preparation of crystalline ITO nanoparticles with uniform particle shape and size in the range of about 10 nm has not yet been achieved. Recent work on the synthesis of metal oxide nanoparticles gave some strong evidence that on that small size scale nonaqueous reaction approaches are particularly successful.[24] In comparison to reactions in aqueous media, the synthesis of metal oxide nanoparticles in organic solvents provides better control over particle size, shape, crystallinity, and surface properties. However, the main advantage lies in the accessibility of highly crystalline products at moderate temperatures. This feature is strongly related to the fact that switching from aqueous sol−gel chemistry and its high reactivity of water to nonhydrolytic processes drastically decreases the reaction rates and leads to controlled crystallization. A large number of metal oxide nanoparticles have been prepared on the basis of these routes, some of them relying on the use of surfactants as size and shape controlling agents[25−27] and some of them just taking advantage of the stabilizing effect of the organic solvents.[28−35]

Here we present a nonaqueous route to ITO nanoparticles with variable tin oxide content involving the solvothermal reaction of indium acetylacetonate and tin *tert*-butoxide in benzyl alcohol. The methodology presented here is particularly attractive for several reasons: (i) all precursors are commercially available; (ii) it is a simple one pot reaction; (iii) there is by concept no contamination with halide ions; (iv) the as-synthesized nanoparticles are highly crystalline, nearly spherical in shape, and with narrow size distribution; and (v) the nanoparticles show good electrical conductivity without any postannealing steps.

Experimental Details

Materials. Indium(III) acetylacetonate (99.99+%), tin(IV) *tert*-butoxide (99.99+%), and anhydrous benzyl alcohol (99.8%) were obtained from Aldrich and used as received. The solvothermal treatment was performed in Parr acid digestion bombs with 45 mL Teflon cups.

Synthesis. The synthesis was started in a glovebox. As a representative example, the protocol for ITO nanoparticles with 15 wt % SnO_2 is given (ITO-15). A total of 1.53 mmol of $In(acac)_3$ (0.6309 g) and 0.25 mmol $Sn(OtBu)_4$ (0.1023 g) were stirred in a vial with 20 mL of benzyl alcohol for about 1 h. The slightly turbid reaction mixture was transferred into the Teflon lined steel autoclave. The autoclave was taken out of the glovebox and heated at 200 °C for about 48 h in a lab furnace. The ITO particles were collected by centrifugation, washed twice with chloroform, and dried at 60 °C for 12 h in air. All the samples were blue, and the yields were about 40−45%. The SnO_2 content was varied by changing the ratio of the two precursors from 2 wt % (ITO-2) to 30 wt % SnO_2 (ITO-30; see Table 1).

Characterization. The X-ray powder diffraction (XRD) diagrams of all samples were measured in reflection mode (Cu Kα radiation) on a Bruker D8 diffractometer equipped with a scintillation counter. The structural and microstructural parameters were extracted using Rietveld refinement[36] with the program FULL-

(21) Al-Dahoudi, N.; Aegerter, M. A. *J. Sol.-Gel Sci. Technol.* **2003**, *26*, 693−697.
(22) (a) Xu, H.-R.; Zhu, G.-S.; Zhou, H.-Y.; Yu, A.-B. *Mater. Lett.* **2005**, *59*, 19−21. (b) Song, J. E.; Lee, D. K.; Kim, H. W.; Kim, Y. I.; Kang, Y. S. *Colloids Surf., A* **2005**, *257−258*, 539−542.
(23) Kim, S.-M.; Seo, K.-H.; Lee, J.-H.; Kim, J.-J.; Lee, H. Y.; Lee, J.-S. *J. Eur. Ceram. Soc.* **2006**, *26*, 73−80.
(24) Niederberger, M.; Garnweitner, G.; Pinna, N.; Neri, G. *Prog. Solid State Chem.* **2005**, *33*, 59−70.
(25) Cozzoli, P. D.; Kornowski, A.; Weller, H. *J. Am. Chem. Soc.* **2003**, *125*, 14539−14548.
(26) Park, J.; An, K.; Hwang, Y.; Park, J. G.; Noh, H. J.; Kim, J. Y.; Park, J. H.; Hwang, N. M.; Hyeon, T. *Nat. Mater.* **2004**, *3*, 891−895.
(27) Epifani, M.; Arbiol, J.; Díaz, R.; Perálvarez, M. J.; Siciliano, P.; Morante, J. R. *Chem. Mater.* **2005**, *17*, 6468−6472.
(28) Gaskins, B. C.; Lannutti, J. J. *J. Mater. Res.* **1996**, *11*, 1953−1959.
(29) Kominami, H.; Kato, J.; Takada, Y.; Doushi, Y.; Ohtani, B.; Nishimoto, S.; Inoue, M.; Inui, T.; Kera, Y. *Catal. Lett.* **1997**, *46*, 235−240.
(30) Niederberger, M.; Bartl, M. H.; Stucky, G. D. *J. Am. Chem. Soc.* **2002**, *124*, 13642−13643.
(31) (a) Niederberger, M.; Pinna, N.; Polleux, J.; Antonietti, M. *Angew. Chem., Int. Ed.* **2004**, *43*, 2270−2273. (b) Niederberger, M.; Garnweitner, G.; Pinna, N.; Antonietti, M. *J. Am. Chem. Soc.* **2004**, *126*, 9120−9126.
(32) Pinna, N.; Garnweitner, G.; Antonietti, M.; Niederberger, M. *Adv. Mater.* **2004**, *16*, 2196−2200.
(33) Garnweitner, G.; Antonietti, M.; Niederberger, M. *Chem. Commun.* **2005**, 397−399.
(34) Pinna, N.; Garnweitner, G.; Antonietti, M.; Niederberger, M. *J. Am. Chem. Soc.* **2005**, *127*, 5608−5612.
(35) Polleux, J.; Gurlo, A.; Antonietti, M.; Niederberger, M. *Angew. Chem., Int. Ed.* **2006**, *45*, 261−265.
(36) McCusker, L. B.; Von Dreele, R. B.; Cox, D. E.; Louer, D.; Scardi, P. *J. Appl. Crystallogr.* **1999**, *32*, 36−50.

PROF.[37] The scale factor, the background coefficients, the zero point of the detector, and the unit cell parameters were simultaneously refined, followed by the refinement of the Gaussian half width parameters, *U*, *V*, and *W*, and the Lorentzian half width parameters, *X* and *Y*. These parameters define the diffraction profile function, which was chosen to be the modified Thompson−Cox−Hastings pseudo-Voigt,[38] making the size-microstrain analysis straightforward. In the final step, intensity dependent parameters [atomic positions (x_j, y_j, z_j)] were refined. Instrumental profile asymmetry was modeled using asymmetry correction functions with two refinable parameters for 2θ angles lower than 40°. The crystal structure was refined in the space group of In_2O_3, $Ia\bar{3}$ (206). The polynomial function of 2θ of the third order as background resulted in the best fit. The refinement incorporated weights w_i based on the observed step intensities Y_i, $w_i = 1/Y_i$. The refinement was continued until the shift in any parameter, Δx_i, was less than one-third of its estimated standard deviation, σ_i. That convergence criterion was chosen according to the nature of incident radiation (XRD). The quality of Rietveld refinement was evaluated in terms of the discrepancy factor (weighted residual error), R_{wp}, and the goodness-of-fit indicator, GOF. The determination of the volume-weighted average grain sizes (D) and the root-mean-square (rms) lattice microstrain ($\langle \epsilon^2_{hkl} \rangle^{1/2}$) for the ITO phase was achieved by the line-broadening analysis. The instrumental contribution to the peak broadening was removed by the deconvolution method with crystalline α-Al_2O_3 as the standard.

Transmission electron microscopy (TEM) in absorption contrast and high-resolution transmission electron microscopy (HRTEM) in phase contrast were performed at 200 kV on a field-emission instrument of the type JEOL JEM-2100F with an ultrahigh-resolution pole piece, providing a point resolution better than 0.19 nm. An Oxford Instruments INCA-200-TEM system with an ultrathin window was connected to the microscope that allowed elemental analysis using energy-dispersive X-ray spectroscopy (EDXS). Moreover, the microscope was equipped with an energy filter of the type Gatan GIF 2001 with a 1k charge-coupled device camera. The filter was used to enhance the dynamics in the selected area electron diffraction (SAED) pattern by elastic filtering with a bandwidth of 15 eV. The samples were deposited as dry powders on 300-mesh copper-supported carbon films.

X-ray photoelectron spectroscopy (XPS) measurements were taken on a Physical Electronics ESCA 5600 spectrometer with a monochromatic Al Kα X-ray source at a power of 200 W/14 kV and a multichannel detector OmniIV. The electron takeoff angle (θ) to the sample surface was adjusted to 45°. The base pressure of the sample chamber was around 4×10^{-8} Pa throughout the measurements. Spectra were obtained for both high-resolution mode (pass energy of 58.70 eV, 0.125 eV/step) for C 1s, O 1s, Sn 3d, and In 3d and low-resolution mode (pass energy of 187.85 eV, 0.8 eV/step). Binding energies for the high-resolution spectra were calibrated by setting C 1s to 284.6 eV. Gaussian−Lorentzian curves and Shirley background were applied for photoelectron peak analysis.

Conductivity measurements were performed on ITO pellets (13 mm in diameter) prepared from about 120 mg of powder in an evacuated press under a pressure of 10 tons. These cold-pressed pellets were directly used for the measurements without any additional thermal treatment. The pellets were contacted between the gold-plated cylindrical electrodes (Bürklin, 2 mm in diameter) acting both as voltage and current leads. Resistance across the pellet was measured by a digital multimeter (Keithley Instruments, Model 2000) in a four-probe mode for eliminating the undesired resistance of the measuring circuit. The specific conductivity σ was calculated from the measured resistance R as $\sigma = \delta/RS$, where S is the electrode area and δ is the pellet thickness. Annealing experiments were performed on the ITO-15 pellet heated in a furnace at 200, 400, 600, and 700 °C (heating rate of 2 °C/min) under a nitrogen atmosphere.

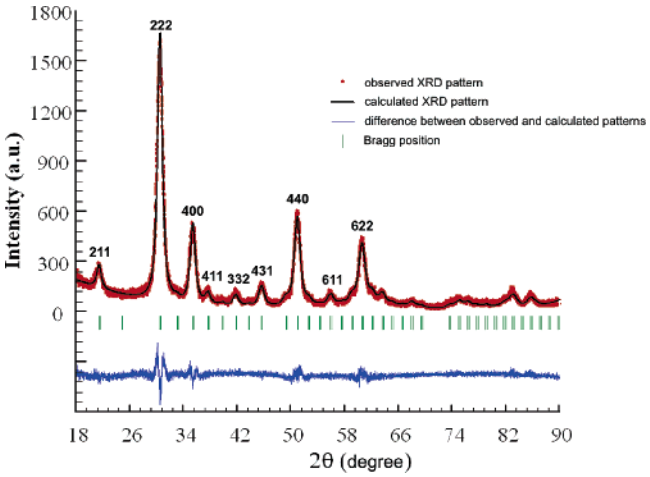

Figure 1. Experimental (red) and calculated (black) XRD patterns of sample ITO-15.

Results and Discussion

The use of benzyl alcohol as the solvent has already proven to be a particularly versatile reaction medium for the nonaqueous and surfactant-free synthesis of metal oxide nanoparticles. Metal oxide precursors such as metal halides, metal alkoxides, and metal acetylacetonates readily react with benzyl alcohol to the corresponding oxides. The particularity in the case of ITO lies in the simultaneous use of the two chemically different precursors indium acetylacetonate and tin *tert*-butoxide. Obviously the reactivity of the precursors in benzyl alcohol matches each other in a way that formation of solid solution takes place, and at the same time the starting In-to-Sn ratio is closely reflected in the final composition of the ITO nanoparticles. This attractive feature enables the controlled preparation of ITO nanoparticles with varying tin oxide content over the range of 2−30 wt % (Table 1). The samples are named according to the starting concentrations; that is, ITO-2 corresponds to an indium acetylacetonate-to-tin *tert*-butoxide ratio of 2 wt % SnO_2 doping in In_2O_3, ITO-6 corresponds to 6 wt % SnO_2, and so on.

Figure 1 displays the experimental XRD pattern of the ITO-15 sample (15 wt % SnO_2 according to the starting concentration) together with the corresponding Rietveld refinement as a representative example for all ITO samples. Independent of the SnO_2 content, the as-synthesized ITO nanoparticles are highly crystalline and all the diffractograms correspond to the cubic bixbyite structure of indium oxide (ICDD PDF No. 6-416) without any indication of crystalline SnO_2 as an additional phase. This observation points to the formation of solid solutions rather than the mixture of indium oxide and tin oxide. The experimental powder diagram and the pattern calculated by Rietveld refinement agree well with each other, confirming the structural model. Numerical values

(37) Rodriguez-Carvajal, J. *FULLPROF-A program for Rietveld Refinement*; Laboratorie Leon Brillouin: CEA-Saclay, France, 2000.
(38) Thompson, P.; Cox, D. E.; Hastings, J. B. *J. Appl. Crystallogr.* **1987**, *20*, 79−83.

of the weighted residual error (R_{wp}) are in the range from 12.0 to 14.7%, and the values of the goodness-of-fit indicator (GOF) are 1.3 and 1.4, which corroborates the quality of the fit.

Rietveld refinement calculations also provide crystallographic information regarding crystallite sizes, microstrains, and the lattice parameter. These results are summarized in Table 1 and listed in more detail in Table 2 in Supporting Information. The crystallite sizes were additionally determined by the Scherrer equation[39] from the line broadening of the (222) reflection. With increasing SnO_2 content, the crystallite sizes gradually decrease from 17.9 nm (ITO-2) to 7.6 nm (ITO-30; Table 1), while at the same time the rms microstrain increases (see Table 2 in Supporting Information). This result implies that the lattice defects increase together with the doping level, which clearly demonstrates the influence of the tin atoms on the formation of ITO crystallites. In this context it is interesting to recall that pure indium oxide nanoparticles obtained in benzyl alcohol exhibit a cubelike particle shape with an average side length of 20 nm.[40] The results of comprehensive size-microstrain analysis confirm this trend to smaller particle sizes with higher SnO_2 doping, however with slightly smaller crystallite sizes than the ones obtained from Scherrer analysis (Table 1). The drop in size with increasing SnO_2 content coincides well with the literature.[41] In the case of the calculated lattice parameters it is difficult to observe any clear tendencies. The lattice parameters increase from ITO-2 to ITO-8, reaching a maximum at ITO-10, followed by a slight decrease for ITO-12 and ITO-15. However, all these ITO samples exhibit a larger lattice parameter than that of pure In_2O_3, $a = 10.118$ Å (ICDD PDF No. 6-416), giving additional evidence for the incorporation of Sn^{4+} into the indium oxide lattice and, thus, for formation of solid solutions. The observed increase in the lattice parameter is consistent with the data reported in the literature,[42] although it contradicts Vegard's law predicting a linear decrease in the lattice parameter as the tin content increases as a result of the smaller ionic radius of Sn^{4+} compared to that of In^{3+}. The increase of the lattice parameter is attributed to the larger repulsive forces arising from the additional positive charge of the tin cations.[43] To balance this extra charge, free electrons are released into the conduction band, increasing carrier concentration and consequently resulting in higher conductivity.[44] Another effect associated with tin doping is the presence of oxygen interstitials on the vacant anionic sites (denoted as O(2) in Table 2 in Supporting Information),[42] which are always empty in pure In_2O_3. In our solvothermally prepared samples the occupation of interstitial oxygen vacancies is always observed and reaches up to 18.3% for ITO-8. These oxygen interstitial anions partially compensate the extra Sn^{4+} positive charge but also influence the ion−ion distance distorting the In/Sn−O octahedron (see Table 2 in Supporting Information).

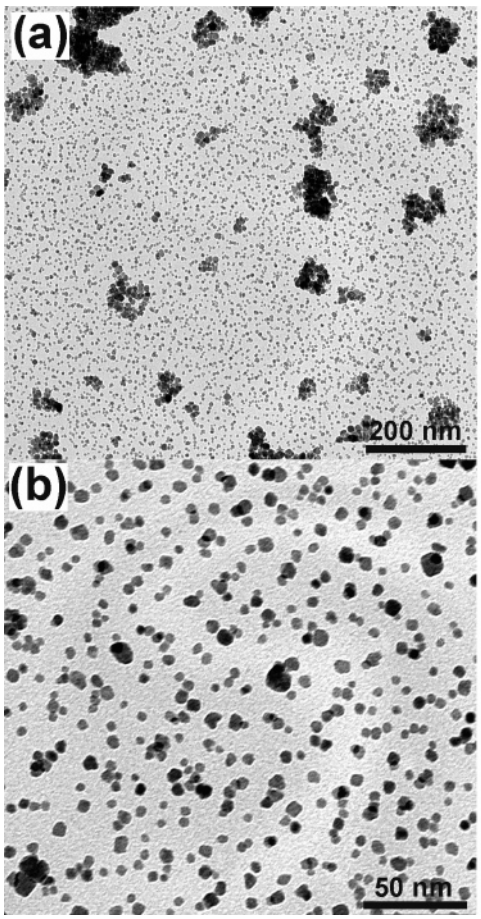

Figure 2. TEM overview images of sample ITO-10 at different magnifications.

On the other hand, for ITO-20, ITO-25, and ITO-30 the lattice parameters are considerably smaller (Table 1). Regarding this observation the data in the literature is controversial, probably because of the fact that the Sn^{4+} ions have the choice between two different indium sites. Depending on whether they occupy the In1 or In2 positions the influence on the oxygen stoichiometry, the lattice parameters, and the bond lengths is different.[41,42,45]

As a representative example, TEM micrographs of sample ITO-10 are shown in Figure 2. An overview image (Figure 2a) illustrates that in addition to individual particles, also some agglomerates are present. A closer view on the area with well-dispersed particles demonstrates that the particle size distribution is in the range of 5−10 nm (Figure 2b), which is in good agreement with the Rietveld data. The particles not only are characterized by a relatively narrow particle size distribution but also exhibit a nearly spherical and uniform particle morphology.

Further studies on samples ITO-10 and ITO-15 by HR-TEM and EDXS gave additional insight into the crystal structure. Figure 3a depicts an SAED pattern of ITO-15 from a circular region of approximately 550 nm in diameter. The

(39) Klug, H. P.; Alexander, L. E. *X-ray Diffraction Procedures: For Polycrystalline and Amorphous Materials*; Wiley-Interscience: New York, 1974.
(40) Pinna, N.; Neri, G.; Antonietti, M.; Niederberger, M. *Angew. Chem., Int. Ed.* **2004**, *43*, 4345−4349.
(41) Quaas, M.; Eggs, C.; Wulff, H. *Thin Solid Films* **1998**, *332*, 277−281.
(42) Nadaud, N.; Lequeux, N.; Nanot, M.; Jove, J.; Roisnel, T. *J. Solid State Chem.* **1998**, *135*, 140−148.
(43) Frank, G.; Köstlin, H. *Appl. Phys. A* **1982**, *27*, 197−206.
(44) Freeman, A. J.; Poeppelmeier, K. R.; Mason, T. O.; Chang, R. P. H.; Marks, T. J. *MRS Bull.* **2000**, *25*, 45−51.
(45) Gonzalez, G. B.; Cohen, J. B.; Hwang, J. H.; Mason, T. O.; Hodges, J. P.; Jorgensen, J. D. *J. Appl. Phys.* **2001**, *89*, 2550−2555.

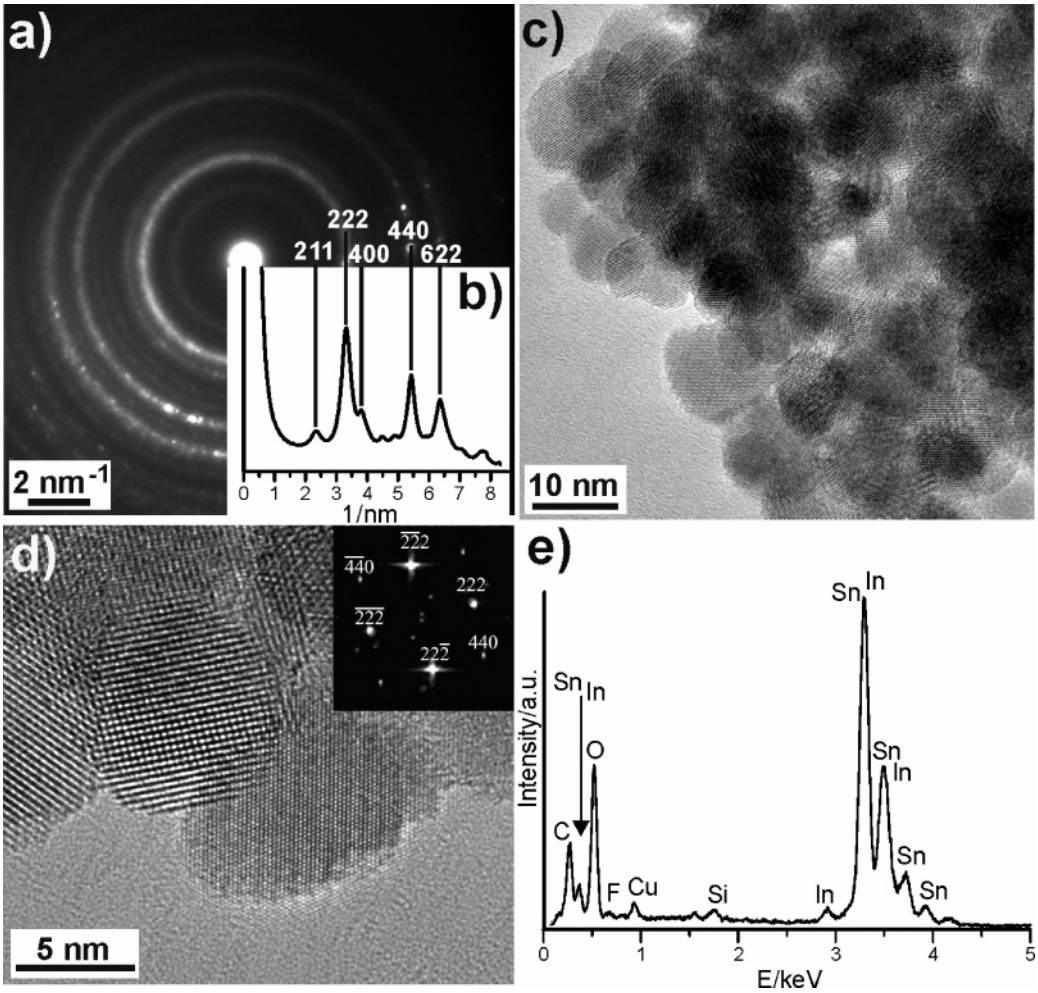

Figure 3. (a) SAED pattern of sample ITO-15 and (b) its corresponding radial intensity distribution, (c and d) HRTEM micrographs of sample ITO-10 (inset, power spectrum), and (e) EDXS spectrum of sample ITO-10.

Debye−Scherrer rings clearly indicate the polycrystalline nature of the powder. The radial intensity diagram in Figure 3b perfectly matches the XRD pattern of sample ITO-15 (Figure 1) and illustrates that cubic bixbyite structure is the only crystal structure existing in the specimen. Several SAED measurements on different areas of the sample always resulted in the same SAED pattern, giving strong evidence for solid solution formation of indium oxide and tin oxide. The HRTEM images of sample ITO-10 at different magnifications are shown in Figure 3c,d. The well-developed lattice fringes are randomly oriented, which prove the high crystallinity of the sample and random orientation of the nanoparticles with respect to one another. The grain boundaries are clearly visible on these HRTEM images, confirming a crystallite size of sample ITO-10 predominantly in the range from 5 to 10 nm. It is a notable feature that every particle consists of just one domain without any internal grain boundaries, which gives additional evidence for solid solution formation, but also clearly shows the single crystalline nature of every particle. The power spectrum of the nanocrystal (shown in the middle of Figure 3d) is characteristic of a particle oriented along the [$\bar{1}$10] direction (Figure 3d, inset).

The EDX spectrum of sample ITO-10 is presented in Figure 3e. Because of the closely related atomic number the peaks of indium and tin always overlap, which makes quantitative analysis by EDXS impossible. In addition to indium, tin, oxygen, and carbon as main species, also copper (from the TEM grid) and traces of silicon and fluorine were detected.

To gain further insights into the chemical composition and into the atomic ratio of In, Sn, and O in the ITO nanoparticles, the samples were analyzed by means of XPS. These measurements also provide information about the final composition of the ITO nanoparticles, that is, the final concentration of the SnO_2 doping in In_2O_3, with respect to the starting indium acetylacetonate-to-tin *tert*-butoxide ratio, a crucial issue for synthesis planning.

As representative examples, ITO-2, ITO-10, and ITO-15 were investigated. In consideration of the fact that the usual X-ray penetration depth is about 2−3 nm at an electron takeoff angle of $\theta = 45°$ and that the samples are highly homogeneous with small and uniform particle sizes, it is reasonable to regard the obtained data as characteristic for the whole specimen. Figure 4a shows the typical survey spectrum of ITO, and these are similar for all three samples. Apart from a C 1s peak positioned at 284.6 eV, which stems from carbon containing molecules adsorbed onto the nanoparticle surface (mainly benzyl alcohol and its derivatives),[46] only In, Sn, and O related core levels were detected, proving

(46) Polleux, J.; Pinna, N.; Antonietti, M.; Hess, C.; Wild, U.; Schlögl, R.; Niederberger, M. *Chem.−Eur. J.* **2005**, *11*, 3541−3551.

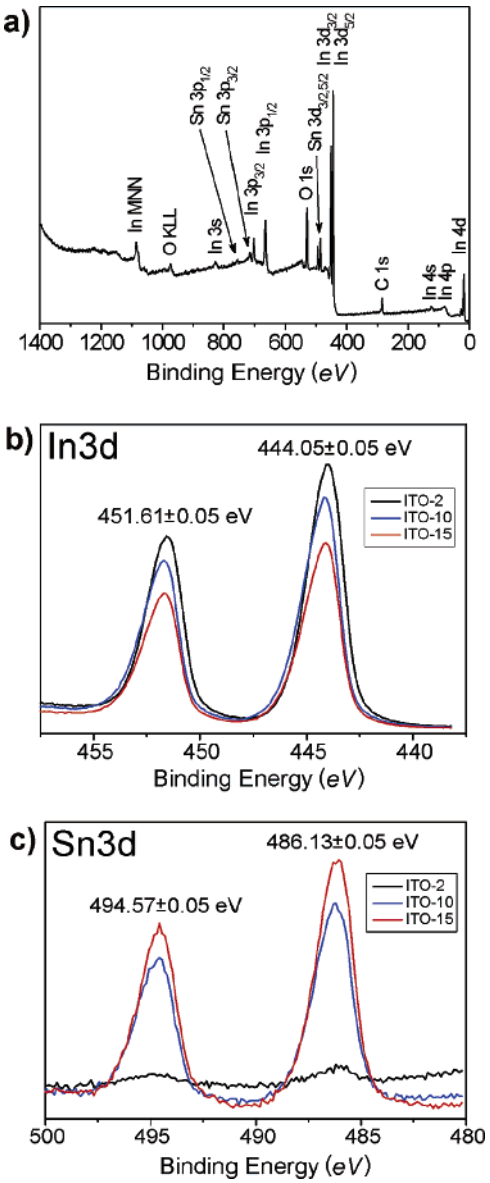

Figure 4. XPS investigations of ITO-2, ITO-10, and ITO-15. (a) Survey spectrum (similar for all three samples), (b) high-resolution In 3d spectrum, and (c) high-resolution Sn 3d spectrum of the core levels.

the high purity of the samples. Besides the wide-scan, high-resolution spectra of the In 3d (Figure 4b), Sn 3d (Figure 4c), O 1s, and C 1s regions were recorded at three different locations of every sample. Because of so-called "final-state" effects, the In 3d and Sn 3d region consists of a single doublet at binding energies of 451.6 eV for In $3d_{3/2}$ and 444.1 eV for In $3d_{5/2}$ and 494.6 eV for Sn $3d_{3/2}$ and 486.1 eV for Sn $3d_{5/2}$. These values are in good agreement with literature data.[47] The positions of the In 3d and Sn 3d peaks as well as the symmetry of the line shape strongly point to the exclusive presence of both species in the oxidation states III and IV, respectively, without any indication for the formation of metallic components. Calculations of the areas of the In $3d_{5/2}$ and Sn $3d_{5/2}$ emission lines (sensitivity factors: 4.51 for In $3d_{5/2}$ and 4.89 for Sn $3d_{5/2}$) resulted in the atomic In-to-Sn ratio of 146.1 for ITO-2, 10.53 for ITO-10, and 6.71 for ITO-15, which is generally slightly smaller as compared to the starting recipes. In the case of ITO-2, the tin concentration is close to the detection limit of XPS, which leads to a relatively large error. All these data are summarized in Table 1. Measurements for the estimation of the O-to-(In, Sn) ratio were also performed at three different positions of the samples. The acquired data for the O 1s region revealed a peak with a slight hump on the high energy side. Hence, the O 1s spectrum was deconvoluted into two components at 529.6 and 530.7 eV, corresponding to bulk oxygen of ITO and to the OH group of benzyl alcohol on the surface of the nanoparticles, respectively. The peak analysis revealed certain oxygen sub-stoichiometry, which is indicative of the presence of oxygen vacancies. These vacancies contribute to the electron conductivity, providing the high concentration of free electrons, which also explains the dark blue color of the ITO nanoparticles.[44] The precise determination of the oxygen stoichiometry by XPS is, however, not possible. Investigations of the valence band structure of ITO revealed a band gap of about 3.3−3.4 eV and a slight hump at about 1.5−3 eV, which is usually correlated to the improved conductivity of ITO[48] and could provide an explanation for the good conductivity of the nanoparticles. In conclusion, the XPS investigations were indicative for the formation of chemically pure, n-type semiconductive ITO nanoparticles with SnO_2 content up to 15 wt %, which is considerably higher than the solubility limit of 6 atom % reported for bulk ITO.[49]

The results of the electrical conductivity measurements performed on pelletized ITO nanopowders with different SnO_2 contents are summarized in Table 1. Figure 5a represents these measurements graphically by plotting the tin oxide content (based on the starting concentrations) versus specific conductivity. The change of conductivity is not linear but follows a trend often observed for ITO materials.[2,42] With increasing SnO_2 doping also the conductivity of the ITO samples gradually increases, because of the higher level of electron doping, reaching a maximum at 15 wt % of SnO_2. However, larger SnO_2 concentrations lead to a drastic drop in the conductivity of about 70−80% compared to the maximum value. This observation is attributed to the formation of stable tin−oxygen associates for high tin doping levels, which do not contribute to the electrical conduction.[14,18,45,50−52] Because all of our ITO samples are highly crystalline, the change in the electrical properties of the various samples is mainly a consequence of the variation of the electron doping level in their lattice and not of the degree of crystallinity. One has to note that the optimum Sn doping level of 15 wt % associated with the maximum conductivity

(47) Moulder, J. F.; Stickle, W. F.; Sobol, P. E.; Bomben, K. D. *Handbook of X-ray Photoelectron Spectroscopy: A Reference Book of Standard Spectra for Identification and Interpretation of XPS Data*; Physical Electronics Division, Perkin-Elmer Corp.: Eden Prairie, MN, 1992.

(48) Pujilaksono, B.; Klement, U.; Nyborg, L.; Jelvestam, U.; Hill, S.; Burgard, D. *Mater. Charact.* **2005**, *54*, 1−7.

(49) Frank, G.; Köstlin, H.; Rabenau, A. *Phys. Status Solidi A* **1979**, *52*, 231−238.

(50) Parent, P.; Dexpert, H.; Tourillon, G.; Grimal, J. M. *J. Electrochem. Soc.* **1992**, *139*, 282−285.

(51) Hwang, J. H.; Edwards, P. P.; Kammler, H. K.; Mason, T. O. *Solid State Ionics* **2000**, *129*, 135−144.

(52) Gonzalez, G. B.; Mason, T. O.; Quintana, J. P.; Warschkow, O.; Ellis, D. E.; Hwang, J. H.; Hodges, J. P.; Jorgensen, J. D. *J. Appl. Phys.* **2004**, *96*, 3912−3920.

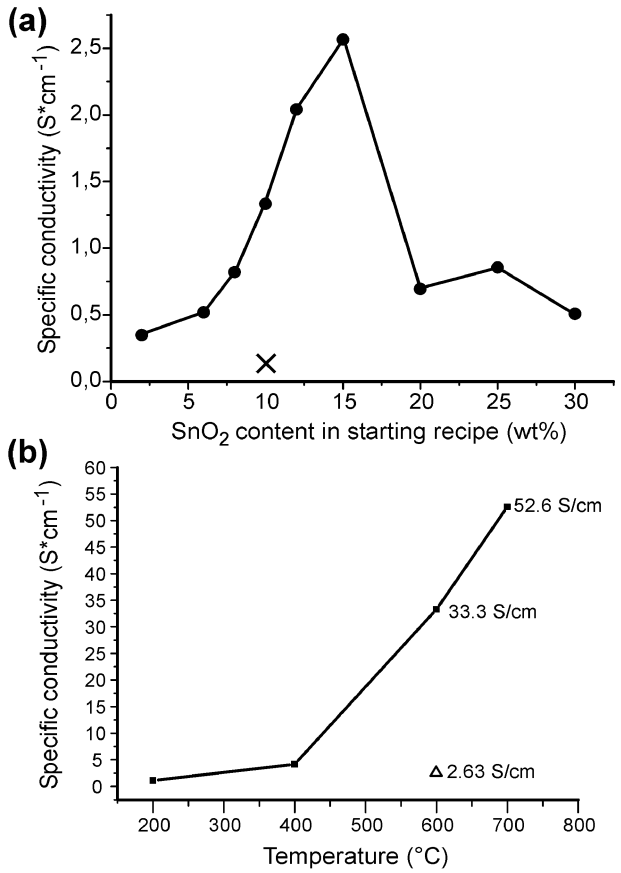

Figure 5. (a) Specific conductivity of the solvothermally prepared ITO nanopowders in dependence of the initial Sn content, together with commercially available ITO nanopowders (Aldrich, 10 wt % SnO_2) as a comparison (cross). (b) Specific conductivity of ITO-15 in dependence of the annealing temperature.

is higher than the majority of the values reported in the literature for ITO. Apart from some exceptions (e.g., 17 wt % of SnO_2 in ITO films prepared by the evaporation technique[10]) the optimum SnO_2 content was generally reported to be in the range of 5−12 wt %, depending on the preparation method and preparation conditions.[53−55] The higher optimum SnO_2 level in ITO nanoparticles prepared by our method might indicate the larger solubility and better distribution of tin in the indium oxide matrix compared to the conventionally prepared ITO materials. This feature is usually attributed to the nonequilibrium preparation conditions that prevent tin from forming a segregate oxide phase.[50] In comparison to commercially available ITO powders (Aldrich, 10 wt % SnO_2, 25−45 nm mean particle size) measured under similar conditions, the conductivity of our ITO samples is almost 1 order of magnitude higher. Figure 5a shows that the two samples with 10 wt % SnO_2 exhibit a conductivity of 1.33 S/cm for our solvothermally prepared ITO and 0.15 S/cm for the commercial one. As mentioned before, the blue color of all the nanoparticles points to the presence of a high concentration of charge carriers in the conduction band,[56] generated both by oxygen vacancies and by reduction of donor Sn species under removal of interstitial oxygen ions. This observation is additionally confirmed by the fact that annealing of the ITO-15 pellet in air at 600 °C leads to a slight decrease in conductivity (Figure 5b, Δ) as a result of saturation of the oxygen vacancies and oxidation of activated donor species, leveling the expected improvement in conductivity due to sintering of the particles and decreasing of the grain boundary effects. On the other hand, heat treatment of the ITO-15 pellets under a nitrogen atmosphere increases the conductivity, with a pronounced jump to 52.6 S/cm in the range of 400−700 °C (Figure 5b).

However, the maximum conductivity of 2.56 S/cm and 52.6 S/cm for as-synthesized and annealed 15 wt % SnO_2, respectively, is still far below the reported values of up to 1×10^4 S/cm for dense ITO films.[3] The main reason for the lower conductivity lies in the charge scattering on the grain boundary contacts between the nanoparticles. One has to keep in mind that the values obtained from the measurements of the as-synthesized powders without thermal treatment can be considered as the apparent conductivity of the particle ensemble, and they are expected to be much lower than the real bulk conductivity of the ITO lattice of a single particle. Because just the mixture of indium and tin oxides as separated phases is not conductive, the good conductivity of the ITO samples strongly confirms the presence of solid solution formation.

Conclusions

The solvothermal reaction between indium acetylacetonate and tin *tert*-butoxide in benzyl alcohol provides a comfortable nonaqueous route to crystalline ITO nanoparticles with uniform spherical shape and sizes in the range of 5−10 nm. The simple variation of the tin oxide content from 2 to 30 wt % enables the preparation of this TCO with a maximum electrical conductivity at a doping level of 15 wt % of 2.56 S/cm, which is 1 order of magnitude higher than for commercially available nanopowders. Although ITO is well established in the form of thin films obtained by various chemical and physical deposition techniques, the synthesis of ITO powders consisting of nanoparticulate components with the highest possible purities, small crystallite sizes, and well-defined particle morphologies with narrow size distributions is of particular technological interest. The reasons lie in the low cost and ease of processing of nanopowders into thin films, ceramics, and composites, at the same time offering the highest flexibility in terms of substrate structure and geometry. These are all key issues on the way to commercialization of nanoparticles as building blocks for device fabrication.

Acknowledgment. The authors thank the Max Planck Society and Deutsche Forschungsgemeinschaft (DFG; Project Nos. WA 1116/10 and 436 TSE/130/46/0-1) for financial support. The authors are grateful to Wolfgang Rogge (University of Hannover) for help with conductivity measurements.

Supporting Information Available: Structural results and refinement parameters obtained from Rietveld analysis of the XRD data of ITO-2 to ITO-10 (PDF). This material is available free of charge via the Internet at http://pubs.acs.org.

CM060548Q

(53) Alam, M. J.; Cameron, D. C. *Thin Solid Films* **2000**, *377*, 455−459.
(54) Seki, S.; Sawada, Y.; Nishide, T. *Thin Solid Films* **2001**, *388*, 22−26.
(55) Ramanan, S. R. *Thin Solid Films* **2001**, *389*, 207−212.
(56) Lee, J.-S.; Choi, S.-C. *J. Eur. Ceram. Soc.* **2005**, *25*, 3307−3314.